Decentralized $\mathcal{H}_\infty$ Controller Design for Large-scale Civil Structures

Yang Wang [a]*, Jerome P. Lynch [b], Kincho H. Law [c],

[a] School of Civil and Environmental Engineering, Georgia Institute of Technology
Atlanta, GA 30332
[b] Department of Civil and Environmental Engineering, University of Michigan
Ann Arbor, MI 48109
[c] Department of Civil and Environmental Engineering, Stanford University
Stanford, CA 94305

* Yang Wang, Assistant Professor
School of Civil and Environmental Engineering
Georgia Institute of Technology
790 Atlantic Dr NW
Atlanta, GA 30332-0355
Phone: (001) 404-894-1851 Fax: (001) 404-894-2278
Email: yang.wang@ce.gatech.edu

ABSTRACT

Complexities inherent to large-scale modern civil structures pose as great challenges in the design of feedback structural control systems for dynamic response mitigation. For example, system designers now face the difficulty of constructing complicated structural control systems which may contain hundreds, or even thousands, of sensors and control devices in a single system. Key issues in such large-scale structural control systems include reduced system reliability, increasing requirements on communication, and longer latencies in the feedback loop. To effectively address these issues, decentralized control strategies provide promising solutions that allow control systems to operate at high nodal counts. This paper examines the feasibility of designing a decentralized controller that minimizes the $\mathcal{H}_\infty$ norm of the closed-loop system. $\mathcal{H}_\infty$ control is a natural choice for decentralization because imposition of decentralized architectures is easy to achieve when posing the controller design using linear matrix inequalities. Decentralized control solutions are proposed herein for both continuous-time and discrete-time $\mathcal{H}_\infty$ formulations. Detailed procedures for the design of the decentralized $\mathcal{H}_\infty$ controller are first illustrated through a 3-story structure. Performance of the decentralized $\mathcal{H}_\infty$ controller is compared to the performance of another decentralized controller based on the linear quadratic regulator (LQR) optimization criteria. Numerical simulations of the decentralized $\mathcal{H}_\infty$ control solution are then conducted for a 20-story benchmark structure using different decentralized system architectures. Simulations using both ideal and realistic structural control devices illustrate the feasibility of the decentralized $\mathcal{H}_\infty$ control solution.

Keywords: H-infinity control, feedback structural control, decentralized control, smart structures.

1. INTRODUCTION

Real-time feedback control has been a topic of great interest to the structural engineering community over the last few decades [1-4]. A feedback structural control system includes an integrated network of sensors, controllers, and control devices that are installed in the civil structure to mitigate undesired vibrations during external excitations, such as earthquakes or typhoons. Under an external excitation, the dynamic response of the structure is measured by sensors. This sensor data is communicated to a centralized controller that uses the data to calculate an optimal control solution. The optimal solution is then dispatched by the controller to control devices which directly (*i.e.* active devices) or indirectly (*i.e.* semi-active devices) apply forces to the structure. This process repeats continuously in real time to mitigate, or even eliminate, undesired structural vibrations. Typical devices for feedback structural control include semi-active hydraulic dampers (SHD), magnetorheological (MR) dampers, active mass dampers (AMD), among others. It was recently reported that more than 50 buildings and towers have been successfully instrumented with various types of structural control systems from 1989 to 2003 [5].

Traditional feedback structural control systems employ centralized architectures. In such an architecture, one central controller is responsible for collecting data from all the sensors in the structure, making control decisions, and dispatching these control decisions to control devices. Hence, the requirements on communication range and data transmission bandwidth increase with the size of the structure and with the number of sensors and control devices being deployed. These communication requirements could result in great economical and technical difficulties for the application of feedback control systems in increasingly larger civil structures. Furthermore, the centralized controller itself is a single point of potential failure; failure of the controller may paralyze the whole control system. In order to overcome these inherent challenges, decentralized control architectures could be alternatively adopted [6-8]. For example, a structural control system consisting of 88 fully decentralized semi-active oil dampers has been installed in the 170m-tall Shiodome Tower in Tokyo, Japan [9]. In a decentralized control system architecture, multiple controllers are distributed throughout the structure. Acquiring data only from a local sub-set of sensors, each controller commands control devices in its vicinity. The benefits of localizing a sub-set of sensors and control devices to each controller include the need for shorter communication ranges and reduced data transmission rates in the control system. Decentralization also eliminates the risk of global control system failure if one of the controllers should fail.

Decentralized control design based on the linear quadratic regulator (LQR) optimization criteria has been previously explored by the authors to study the feasibility of utilizing wireless sensors as controllers for feedback structural control [10; 11]. This paper investigates a different approach to the design of a decentralized control system based on $\mathcal{H}_\infty$ control theory, which is known to offer excellent control performance when "worst-case" external disturbances are encountered. Due to the multiplicative property of the $\mathcal{H}_\infty$ norm [12], $\mathcal{H}_\infty$ control design is also convenient for representing modeling uncertainties (as is typical in most civil structures). Centralized $\mathcal{H}_\infty$ controller implementation in the continuous-time domain for civil structural control has been extensively studied [13-19].

Previous research illustrates the feasibility and effectiveness of centralized $\mathcal{H}_\infty$ control for civil structures. It has been shown that when compared with traditional linear quadratic Gaussian (LQG) controllers, $\mathcal{H}_\infty$ controllers can achieve either comparable or even superior performance [20; 21]. However, decentralized $\mathcal{H}_\infty$ controller design, either in the continuous time domain or discrete time domain, has rarely been explored by the community.

One important feature of $\mathcal{H}_\infty$ control is that the control solution can be formulated as an optimization problem with constraints expressed by linear matrix inequalities (LMI) [22]. For such problems, sparsity patterns can be easily applied to the controller matrix variables. This property offers significant convenience for designing decentralized controllers, where certain sparsity patterns can be applied to the gain matrices consistent with certain desired feedback architecture. This paper present pilots studies investigating the feasibility of decentralized $\mathcal{H}_\infty$ control that may be employed in large-scale structural control systems. More specifically, decentralized $\mathcal{H}_\infty$ controller design is presented in both the continuous-time and discrete-time domains. Using properties of LMI, the decentralized $\mathcal{H}_\infty$ control problem is converted into a convex optimization problem that can be conveniently solved using available mathematical packages.

Numerical simulations are conducted to validate the performance of the proposed controller design. In the first example, a 3-story structure is used to demonstrate the detailed procedure for the design of the decentralized $\mathcal{H}_\infty$ controller. The control performance of decentralized $\mathcal{H}_\infty$ controllers is then compared with the performance of decentralized LQR-based controllers [10; 11]. In the second example, simulations of a 20-story benchmark structure are conducted to illustrate the efficacy of the decentralized $\mathcal{H}_\infty$ control solution for large-scale civil structures. Different information feedback architectures and control sampling rates are employed so as to provide an in-depth study of the proposed approaches. Control performance using ideal actuators and large-capacity semi-active hydraulic (SHD) dampers are presented for the 20-story structure. Performance of the decentralized control system is compared with passive control cases where the SHD dampers are fixed at minimum or maximum damping settings.

2. FORMULATION OF DECENTRALIZED $\mathcal{H}_\infty$ CONTROL

This section first discusses the design of a decentralized $\mathcal{H}_\infty$ controller for structural control in the continuous-time domain. The controller's counterpart in the discrete-time domain is then derived. In both derivations, properties of linear matrix inequalities are utilized to conveniently convert the formulation of the decentralized control design problem into a convex optimization problem that can be solved by available mathematical packages.

2.1. Continuous-time decentralized $\mathcal{H}_\infty$ control

For a lumped-mass structural model with n degrees-of-freedom (DOF) and controlled by m_2 control devices, the equations of motion can be formulated as:

$$\mathbf{M}\ddot{\mathbf{q}}(t)+\mathbf{C}\dot{\mathbf{q}}(t)+\mathbf{K}\mathbf{q}(t)=\mathbf{T}_\mathbf{u}\mathbf{u}(t)+\mathbf{T}_\mathbf{w}\mathbf{w}(t) \tag{1}$$

where $\mathbf{q}(t)\in\mathbb{R}^{n\times 1}$ is the displacement vector relative to the ground; $\mathbf{M}$, $\mathbf{C}$, $\mathbf{K}\in\mathbb{R}^{n\times n}$ are the mass, damping, and stiffness matrices, respectively; $\mathbf{u}(t)\in\mathbb{R}^{m_2\times 1}$ and $\mathbf{w}(t)\in\mathbb{R}^{m_1\times 1}$ are the control force and external excitation vectors, respectively; and $\mathbf{T}_\mathbf{u}\in\mathbb{R}^{n\times m_2}$ and $\mathbf{T}_\mathbf{w}\in\mathbb{R}^{n\times m_1}$ are the external excitation and control force location matrices, respectively.

For simplicity, the discussion is based on a 2-D shear-frame structure subject to unidirectional ground excitation. In the example structure shown in Figure 1, it is assumed that the external excitation, $\mathbf{w}(t)$, is a scalar ($m_1 = 1$) containing the ground acceleration time history $\ddot{q}_g(t)$; the spatial load pattern $\mathbf{T}_\mathbf{w}$ is then equal to $-\mathbf{M}\{\mathbf{1}\}_{n\times 1}$. Entries in $\mathbf{u}(t)$ are defined as the control forces between neighboring floors. For the 3-story structure, if a positive control force is defined to be moving the floor above the device towards the left direction, and moving the floor below the device towards the right direction (as shown in Figure 1), the control force location matrix $\mathbf{T}_\mathbf{u}$ is defined as:

$$\mathbf{T}_\mathbf{u}=\begin{bmatrix}-1 & 1 & 0\\ 0 & -1 & 1\\ 0 & 0 & -1\end{bmatrix} \tag{2}$$

The second-order ordinary differential equation (ODE), Eq. (1), can be converted to a first order ODE by the state-space formulation as follows:

$$\dot{\mathbf{x}}_I(t)=\mathbf{A}_I\mathbf{x}_I(t)+\mathbf{B}_I\mathbf{u}(t)+\mathbf{E}_I\mathbf{w}(t) \tag{3}$$

where $\mathbf{x}_I=\left[\mathbf{q}(t);\dot{\mathbf{q}}(t)\right]\in\mathbb{R}^{2n\times 1}$ is the state vector; $\mathbf{A}_I\in\mathbb{R}^{2n\times 2n}$, $\mathbf{B}_I\in\mathbb{R}^{2n\times m_2}$, and $\mathbf{E}_I\in\mathbb{R}^{2n\times m_1}$ are the system, control, and excitation matrices, respectively:

$$\mathbf{A}_I=\begin{bmatrix}[\mathbf{0}]_{n\times n} & [\mathbf{I}]_{n\times n}\\ -\mathbf{M}^{-1}\mathbf{K} & -\mathbf{M}^{-1}\mathbf{C}\end{bmatrix},\ \mathbf{B}_I=\begin{bmatrix}[\mathbf{0}]_{n\times m_2}\\ \mathbf{M}^{-1}\mathbf{T}_\mathbf{u}\end{bmatrix},\ \mathbf{E}_I=\begin{bmatrix}\{\mathbf{0}\}_{n\times 1}\\ -\{\mathbf{1}\}_{n\times 1}\end{bmatrix} \tag{4}$$

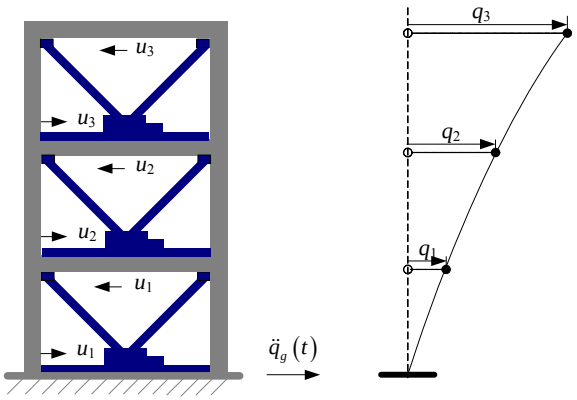

Figure 1. A three-story controlled structure excited by unidirectional ground motion.

In this study, it is assumed that inter-story drifts and velocities are measurable. The displacement and velocity variables in $\mathbf{x}_I$, which are relative to the ground, are first transformed into inter-story drifts and velocities (*i.e.* drifts and velocities between neighboring floors). The inter-story drifts and velocities at each story are then grouped together as:

$$\mathbf{x} = [q_1 \quad \dot{q}_1 \quad q_2 - q_1 \quad \dot{q}_2 - \dot{q}_1 \quad \dots \quad q_n - q_{n-1} \quad \dot{q}_n - \dot{q}_{n-1}]^{\mathrm{T}} \tag{5}$$

A linear transformation matrix $\mathbf{\Gamma} \in \mathbb{R}^{2n \times 2n}$ can be defined such that $\mathbf{x} = \mathbf{\Gamma}\mathbf{x}_I$. Substituting $\mathbf{x}_I = \mathbf{\Gamma}^{-1}\mathbf{x}$ into Eq. (3), and left-multiplying the equation with $\mathbf{\Gamma}$, the state space representation with the transformed (inter-story) state vector becomes:

$$\dot{\mathbf{x}}(t) = \mathbf{A}\mathbf{x}(t) + \mathbf{B}\mathbf{u}(t) + \mathbf{E}\mathbf{w}(t) \tag{6}$$

where

$$\mathbf{A} = \mathbf{\Gamma}\mathbf{A}_I\mathbf{\Gamma}^{-1}, \ \mathbf{B} = \mathbf{\Gamma}\mathbf{B}_I, \ \mathbf{E} = \mathbf{\Gamma}\mathbf{E}_I \tag{7}$$

The system output $\mathbf{z}(t) \in \mathbb{R}^{p \times 1}$ is defined as the sum of linear transformations to the state vector $\mathbf{x}(t)$ and the control vector $\mathbf{u}(t)$:

$$\mathbf{z}(t) = \mathbf{C}_\mathbf{z}\mathbf{x}(t) + \mathbf{D}_\mathbf{z}\mathbf{u}(t) \tag{8}$$

where $\mathbf{C}_\mathbf{z} \in \mathbb{R}^{p \times 2n}$ and $\mathbf{D}_\mathbf{z} \in \mathbb{R}^{p \times m_2}$ are the output matrices for the state and control force vectors, respectively. Assuming static state feedback, the control force $\mathbf{u}(t)$ is determined by $\mathbf{u}(t) = \mathbf{G}\mathbf{x}(t)$, where $\mathbf{G} \in \mathbb{R}^{m_2 \times 2n}$ is termed the control gain matrix. Substituting $\mathbf{G}\mathbf{x}(t)$ for $\mathbf{u}(t)$ in Eq. (6) and Eq. (8), the state-space equations of the closed-loop system can be written as:

$$\begin{cases} \dot{\mathbf{x}}(t) = \mathbf{A}_{CL}\mathbf{x}(t) + \mathbf{E}\mathbf{w}(t) \\ \mathbf{z}(t) = \mathbf{C}_{CL}\mathbf{x}(t) \end{cases} \tag{9}$$

where

$$\begin{cases} \mathbf{A}_{CL} = \mathbf{A} + \mathbf{B}\mathbf{G} \\ \mathbf{C}_{CL} = \mathbf{C}_\mathbf{z} + \mathbf{D}_\mathbf{z}\mathbf{G} \end{cases} \tag{10}$$

In the frequency-domain, the system dynamics can be represented by the transfer function $\mathbf{H}_{\mathbf{zw}}(s) \in \mathbb{C}^{p \times m_1}$ from disturbance $\mathbf{w}(t)$ to output $\mathbf{z}(t)$ as [23]:

$$\mathbf{H}_{\mathbf{zw}}(s) = \mathbf{C}_{CL}(s\mathbf{I} - \mathbf{A}_{CL})^{-1}\mathbf{E} \tag{11}$$

where s is the complex Laplacian variable. The objective of $\mathcal{H}_\infty$ control is to minimize the $\mathcal{H}_\infty$-norm of the closed-loop system, which in the frequency domain is defined as:

$$\left\|\mathbf{H}_{\mathbf{zw}}(s)\right\|_\infty = \sup_\omega \bar{\sigma}\left[\mathbf{H}_{\mathbf{zw}}(\mathrm{j}\omega)\right] \tag{12}$$

where ω represents angular frequency, j is the imaginary unit, $\bar{\sigma}[\bullet]$ denotes the largest singular value of a matrix, and "sup" denotes the supremum (least upper bound) of a set of real numbers. The definition shows that in the frequency domain, the $\mathcal{H}_\infty$-norm of the

system is equal to the peak of the largest singular value of the transfer function $\mathbf{H}_{\mathbf{zw}}(s)$ along the imaginary axis (where $s = j\omega$). The $\mathcal{H}_\infty$ -norm also has an equivalent interpretation in the time domain, as the supremum of the 2-norm amplification from the disturbance to the output:

$$\left\|\mathbf{H}_{\mathbf{zw}}(s)\right\|_\infty = \sup_{\mathbf{w},\|\mathbf{w}(t)\|_2 \neq 0} \left(\left\|\mathbf{z}(t)\right\|_2 / \left\|\mathbf{w}(t)\right\|_2\right) \tag{13}$$

where the 2-norm of a signal $\mathbf{f}(t)$ is defined as $\left\|\mathbf{f}(t)\right\|_2 = \sqrt{\int_{t=-\infty}^{t=+\infty} \mathbf{f}^{\mathrm{T}}(t)\mathbf{f}(t)dt}$, which represents the energy level of a signal. In this study, the $\mathcal{H}_\infty$ -norm can be viewed as the upper limit of the amplification factor from the disturbance (*i.e.* seismic ground motion) energy to the output (*i.e.* structural response) energy. The disturbance is called a "worst-case" disturbance when this upper limit is reached. By minimizing the $\mathcal{H}_\infty$ -norm, the system output (which includes structural response measures) can be greatly reduced when a worst-case disturbance (which is the earthquake excitation) is applied.

According to the Bounded Real Lemma, the following two statements are equivalent for a $\mathcal{H}_\infty$ controller that minimizes the smallest upper bound of the $\mathcal{H}_\infty$ norm of a continuous-time system [22]:

1. $\left\|\mathbf{H}_{\mathbf{zw}}\right\|_\infty < \gamma$ and $\mathbf{A}_{CL}$ is stable in the continuous-time sense (*i.e.* the real parts of all the eigenvalues of $\mathbf{A}_{CL}$ are negative);
2. There exists a symmetric positive-definite matrix $\mathbf{\Theta} \in \mathbb{R}^{2n\times 2n}$ such that following inequality holds:

$$\begin{bmatrix} \mathbf{A}_{CL}\mathbf{\Theta} + \mathbf{\Theta}\mathbf{A}_{CL}{}^T + \mathbf{E}\mathbf{E}^T/\gamma^2 & \mathbf{\Theta}\mathbf{C}_{CL}{}^T \\ * & -\mathbf{I} \end{bmatrix} < 0 \tag{14}$$

where * denotes the symmetric entry (in this case, $\mathbf{C}_{CL}\mathbf{\Theta}$), and "< 0" means that the matrix at the left side of the inequality is negative definite. Using the closed-loop matrix definitions in Eq. (10), Eq. (14) becomes:

$$\begin{bmatrix} \mathbf{A}\mathbf{\Theta} + \mathbf{\Theta}\mathbf{A}^T + \mathbf{B}\mathbf{G}\mathbf{\Theta} + \mathbf{\Theta}\mathbf{G}^T\mathbf{B}^T + \mathbf{E}\mathbf{E}^T/\gamma^2 & \mathbf{\Theta}\mathbf{C}_{\mathbf{z}}{}^T + \mathbf{\Theta}\mathbf{G}^T\mathbf{D}_{\mathbf{z}}{}^T \\ * & -\mathbf{I} \end{bmatrix} < 0 \tag{15}$$

The above nonlinear matrix inequality can be converted into a set of linear matrix inequality (LMI) by introducing a new variable $\mathbf{Y} \in \mathbb{R}^{m_2\times 2n}$ where $\mathbf{Y} = \mathbf{G}\mathbf{\Theta}$:

$$\begin{bmatrix} \mathbf{A}\mathbf{\Theta} + \mathbf{\Theta}\mathbf{A}^T + \mathbf{B}\mathbf{Y} + \mathbf{Y}^T\mathbf{B}^T + \mathbf{E}\mathbf{E}^T/\gamma^2 & \mathbf{\Theta}\mathbf{C}_{\mathbf{z}}{}^T + \mathbf{Y}^T\mathbf{D}_{\mathbf{z}}{}^T \\ * & -\mathbf{I} \end{bmatrix} < 0 \tag{16}$$

In summary, the continuous-time $\mathcal{H}_\infty$ control problem is now transformed into a convex optimization problem:

$$\begin{aligned} &\text{minimize} \quad \gamma \\ &\text{subject to} \quad \mathbf{\Theta} > 0 \text{ and the LMI expressed in Eq. (16)} \end{aligned} \tag{17}$$

Here $\mathbf{Y}$, $\mathbf{\Theta}$, and γ are the optimization variables. Numerical solutions to this optimization problem can be computed, for example, using the Matlab LMI Toolbox [24] or the convex optimization package CVX [25]. After the optimization problem is solved, the control gain matrix is computed as:

$$\mathbf{G} = \mathbf{Y}\mathbf{\Theta}^{-1} \tag{18}$$

In general, the algorithm finds a gain matrix without any sparsity constraints; in other words, it represents a control scheme consistent with a centralized state feedback architecture. To compute gain matrices for decentralized state feedback control, appropriate sparsity constraints can be applied to the optimization variables $\mathbf{Y}$ and $\mathbf{\Theta}$ while solving the optimization problem of Eq. (17). In most available numerical packages, the sparsity constraints can be conveniently defined by assigning corresponding zero entries to the $\mathbf{Y}$ and $\mathbf{\Theta}$ optimization variables. For example, gain matrices of the following sparsity patterns may be employed for a 3-story structure:

$$\mathbf{G}_I = \begin{bmatrix} \blacksquare & 0 & 0 \\ 0 & \blacksquare & 0 \\ 0 & 0 & \blacksquare \end{bmatrix}, \text{ and } \mathbf{G}_{II} = \begin{bmatrix} \blacksquare & \blacksquare & 0 \\ \blacksquare & \blacksquare & \blacksquare \\ 0 & \blacksquare & \blacksquare \end{bmatrix} \tag{19}$$

Note that each entry in the above matrices represents a 1×2 block. According to the linear feedback control law $\mathbf{u}(t) = \mathbf{G}\mathbf{x}(t)$, when the sparsity pattern in $\mathbf{G}_I$ is used, only the inter-story drift and velocity at the i-th story are needed to determine the control force u_i at the same story. When the sparsity pattern in $\mathbf{G}_{II}$ is adopted, the inter-story drifts and velocities from both the i-th story and the neighboring stories (story) are needed in order to determine the control force u_i at the i-th story. Considering the relationship between $\mathbf{G}$ and $\mathbf{Y}$ as specified in Eq. (18), to find control gain matrices satisfying the shape constraints in $\mathbf{G}_I$, the following shape constraints may be applied to the optimization variables $\mathbf{Y}$ and $\mathbf{\Theta}$:

$$\mathbf{Y}_I = \begin{bmatrix} \blacksquare & 0 & 0 \\ 0 & \blacksquare & 0 \\ 0 & 0 & \blacksquare \end{bmatrix}, \text{ and } \mathbf{\Theta}_I = \begin{bmatrix} \blacksquare & 0 & 0 \\ 0 & \blacksquare & 0 \\ 0 & 0 & \blacksquare \end{bmatrix} \tag{20}$$

Similarly, to compute control gain matrices satisfying the shape constraints of $\mathbf{G}_{II}$, the following shape constraints may be applied to the optimization variables:

$$\mathbf{Y}_{II} = \begin{bmatrix} \blacksquare & \blacksquare & 0 \\ \blacksquare & \blacksquare & \blacksquare \\ 0 & \blacksquare & \blacksquare \end{bmatrix}, \text{ and } \mathbf{\Theta}_{II} = \begin{bmatrix} \blacksquare & 0 & 0 \\ 0 & \blacksquare & 0 \\ 0 & 0 & \blacksquare \end{bmatrix} \tag{21}$$

It is important to realize that due to the constraints imposed on the $\mathbf{Y}$ and $\mathbf{\Theta}$ variables, the presented decentralized $\mathcal{H}_\infty$ controller precludes the possibility that a decentralized gain matrix may exist with $\mathbf{Y}$ and $\mathbf{\Theta}$ variables not satisfying the corresponding shape constraints. For example, it is possible that a gain matrix may satisfy the sparsity pattern in $\mathbf{G}_I$ while the corresponding $\mathbf{Y}$ and $\mathbf{\Theta}$ variables do not conform to the sparsity patterns shown in Eq. (20). The application of sparsity patterns to $\mathbf{Y}$ and $\mathbf{\Theta}$ variables makes the gain matrix easily computable using numerical software packages, although the approach may not be able to explore the complete solution space of decentralized gain matrices.

That is, the approach for decentralized $\mathcal{H}_\infty$ controller design may not guarantee that a minimum $\mathcal{H}_\infty$-norm is obtained over the complete solution space; rather, only a minimum $\mathcal{H}_\infty$-norm is obtained for the solution space contained within the boundary imposed by the shape constraints on $\mathbf{Y}$ and $\boldsymbol{\Theta}$.

2.2. Discrete-time decentralized $\mathcal{H}_\infty$ control

For implementation in typical digital control systems, the decentralized $\mathcal{H}_\infty$ control design in discrete-time domain is needed. Using zero-order hold (ZOH) equivalents, the continuous-time system in Eq. (9) can be transformed into an equivalent discrete-time system [26]:

$$\begin{cases} \mathbf{x}_\mathbf{d}[k+1] = \mathbf{A}_{\mathbf{d}CL}\mathbf{x}_\mathbf{d}[k] + \mathbf{E}_\mathbf{d}\mathbf{w}_\mathbf{d}[k] \\ \mathbf{z}_\mathbf{d}[k] = \mathbf{C}_{\mathbf{d}CL}\mathbf{x}_\mathbf{d}[k] \end{cases} \tag{22}$$

where the subscript "d" indicates that the variables are expressed in the discrete-time domain, and the closed-loop system matrices $\mathbf{A}_{\mathbf{d}CL}$ and $\mathbf{C}_{\mathbf{d}CL}$ are defined accordingly:

$$\begin{cases} \mathbf{A}_{\mathbf{d}CL} = \mathbf{A}_\mathbf{d} + \mathbf{B}_\mathbf{d}\mathbf{G}_\mathbf{d} \\ \mathbf{C}_{\mathbf{d}CL} = \mathbf{C}_\mathbf{z} + \mathbf{D}_\mathbf{z}\mathbf{G}_\mathbf{d} \end{cases} \tag{23}$$

For linear state feedback, the control force $\mathbf{u}_\mathbf{d}[k]$ is determined as $\mathbf{u}_\mathbf{d}[k] = \mathbf{G}_\mathbf{d}\mathbf{x}_\mathbf{d}[k]$. According to the Bounded Real Lemma, the following two statements are equivalent for discrete-time systems [23]:

1. The $\mathcal{H}_\infty$-norm of the closed-loop system in Eq. (22) is less than γ, and $\mathbf{A}_{\mathbf{d}CL}$ is stable in the discrete-time sense (*i.e.* all of the eigenvalues of $\mathbf{A}_{\mathbf{d}CL}$ fall in the unit circle on the complex plane);
2. There exists a symmetric matrix $\bar{\boldsymbol{\Theta}}_\mathbf{d} > 0$ such that the following inequality holds:

$$\begin{bmatrix} \mathbf{A}_{\mathbf{d}CL}{}^T & \mathbf{C}_{\mathbf{d}CL}{}^T/\gamma \\ \mathbf{E}_\mathbf{d}{}^T & \mathbf{0} \end{bmatrix} \begin{bmatrix} \bar{\boldsymbol{\Theta}}_\mathbf{d} & \mathbf{0} \\ \mathbf{0} & \mathbf{I} \end{bmatrix} \begin{bmatrix} \mathbf{A}_{\mathbf{d}CL} & \mathbf{E}_\mathbf{d} \\ \mathbf{C}_{\mathbf{d}CL}/\gamma & \mathbf{0} \end{bmatrix} - \begin{bmatrix} \bar{\boldsymbol{\Theta}}_\mathbf{d} & \mathbf{0} \\ \mathbf{0} & \mathbf{I} \end{bmatrix} < 0 \tag{24}$$

Replacing $\bar{\boldsymbol{\Theta}}_\mathbf{d}$ with $\tilde{\boldsymbol{\Theta}}_\mathbf{d}/\gamma^2$ and using the Schur complement [22] and congruence transformation, the above matrix inequality in Eq. (24) can be shown as equivalent to:

$$\begin{bmatrix} \tilde{\boldsymbol{\Theta}}_\mathbf{d} & \mathbf{0} & \mathbf{A}_{\mathbf{d}CL}{}^T\tilde{\boldsymbol{\Theta}}_\mathbf{d} & \mathbf{C}_{\mathbf{d}CL}{}^T \\ * & \gamma^2\mathbf{I} & \mathbf{E}_\mathbf{d}{}^T\tilde{\boldsymbol{\Theta}}_\mathbf{d} & \mathbf{0} \\ * & * & \tilde{\boldsymbol{\Theta}}_\mathbf{d} & \mathbf{0} \\ * & * & * & \mathbf{I} \end{bmatrix} > 0 \tag{25}$$

Left-multiplying and right-multiplying the above matrix with a positive definite matrix $diag(\tilde{\boldsymbol{\Theta}}_\mathbf{d}{}^{-1}, \mathbf{I}, \tilde{\boldsymbol{\Theta}}_\mathbf{d}{}^{-1}, \mathbf{I})$, and letting $\boldsymbol{\Theta}_\mathbf{d} = \tilde{\boldsymbol{\Theta}}_\mathbf{d}{}^{-1}$, the following matrix inequality is obtained:

$$\begin{bmatrix} \boldsymbol{\Theta}_{\mathbf{d}} & \mathbf{0} & \boldsymbol{\Theta}_{\mathbf{d}}\mathbf{A}_{\mathbf{d}CL}{}^{T} & \boldsymbol{\Theta}_{\mathbf{d}}\mathbf{C}_{\mathbf{d}CL}{}^{T} \\ * & \gamma^2\mathbf{I} & \mathbf{E}_{\mathbf{d}}{}^{T} & \mathbf{0} \\ * & * & \boldsymbol{\Theta}_{\mathbf{d}} & \mathbf{0} \\ * & * & * & \mathbf{I} \end{bmatrix} > 0 \tag{26}$$

Similar to the continuous-time system, by replacing the closed-loop matrices $\mathbf{A}_{\mathbf{d}CL}$ and $\mathbf{C}_{\mathbf{d}CL}$ in Eq. (23), and letting $\mathbf{Y}_{\mathbf{d}} = \mathbf{G}_{\mathbf{d}}\boldsymbol{\Theta}_{\mathbf{d}}$, the above matrix inequality can be converted into:

$$\begin{bmatrix} \boldsymbol{\Theta}_{\mathbf{d}} & \mathbf{0} & \boldsymbol{\Theta}_{\mathbf{d}}\mathbf{A}_{\mathbf{d}}^{T} + \mathbf{Y}_{\mathbf{d}}^{T}\mathbf{B}_{\mathbf{d}}^{T} & \boldsymbol{\Theta}_{\mathbf{d}}\mathbf{C}_{\mathbf{z}}^{T} + \mathbf{Y}_{\mathbf{d}}^{T}\mathbf{D}_{\mathbf{z}}^{T} \\ * & \gamma^2\mathbf{I} & \mathbf{E}_{\mathbf{d}}{}^{T} & \mathbf{0} \\ * & * & \boldsymbol{\Theta}_{\mathbf{d}} & \mathbf{0} \\ * & * & * & \mathbf{I} \end{bmatrix} > 0 \tag{27}$$

Therefore, the discrete-time $\mathcal{H}_\infty$ control problem can be converted to a convex optimization problem with LMI constraints:

$$\begin{aligned} &\text{minimize} \quad \gamma \\ &\text{subject to} \quad \boldsymbol{\Theta}_{\mathbf{d}} > 0 \text{ and the LMI expressed in Eq. (27)} \end{aligned} \tag{28}$$

Here again, $\mathbf{Y}_{\mathbf{d}}$, $\boldsymbol{\Theta}_{\mathbf{d}}$, and γ are the optimization variables. After the optimization problem is solved, the control gain matrix is computed as:

$$\mathbf{G}_{\mathbf{d}} = \mathbf{Y}_{\mathbf{d}}\boldsymbol{\Theta}_{\mathbf{d}}^{-1} \tag{29}$$

Furthermore, sparsity patterns of the gain matrix can be achieved by adopting appropriate patterns to the LMI variables $\mathbf{Y}_{\mathbf{d}}$ and $\boldsymbol{\Theta}_{\mathbf{d}}$, as illustrated in the previous description for the continuous-time case.

3. NUMERICAL SIMULATIONS

In section 3.1, a 3-story structure is used to demonstrate the detailed procedures of designing the decentralized $\mathcal{H}_\infty$ controller. Performance of the $\mathcal{H}_\infty$ controllers is compared with the performance of controllers based on the LQR optimization criteria. In section 3.2, simulations using a 20-story benchmark structure are conducted to illustrate the efficacy of the decentralized $\mathcal{H}_\infty$ control solution for large-scale civil structures. Results using both ideal actuators and large-capacity semi-active hydraulic (SHD) dampers are presented for the 20-story structure.

3.1. Numerical simulation of a 3-story structure

3.1.1. Decentralized $\mathcal{H}_\infty$ control

Since the discrete-time formulation is suitable for implementation in modern digital controllers, numerical simulations are conducted using discrete-time $\mathcal{H}_\infty$ controllers formulated by the procedures laid out in Section 2.2. Simulations of a 3-story shear-frame structure are first introduced to illustrate the detailed procedures of decentralized $\mathcal{H}_\infty$ control design. As shown in the formulation, the building is modeled as an in-plane

lumped-mass shear structure with one actuator allocated between every two neighboring floors. It is assumed that both the inter-story drifts and inter-story velocities between every two neighboring floors are measurable. Such an assumption is reasonable considering that modern semi-active hydraulic dampers contain internal stroke sensors and load cells that measure real-time damper displacements and forces, respectively [27]. Assuming a V-brace element like those in Figure 1, the displacement and force measurements can be used to estimate inter-story drift and velocity. The example structure used herein has the following mass, stiffness, and damping matrices:

$$\mathbf{M} = \begin{bmatrix} 6 & & \\ & 6 & \\ & & 6 \end{bmatrix} \times 10^3 \text{ kg}, \quad \mathbf{K} = \begin{bmatrix} 3.4 & -1.8 & \\ -1.8 & 3.4 & -1.6 \\ & -1.6 & 1.6 \end{bmatrix} \times 10^6 \text{ N/m}, \quad \mathbf{C} = \begin{bmatrix} 12.4 & -5.16 & \\ -5.16 & 12.4 & -4.59 \\ & -4.59 & 7.20 \end{bmatrix} \times 10^3 \text{ N/(m/s)} \tag{30}$$

When the external excitation is unidirectional ground motion, the continuous-time system matrices **A**, **B**, **E** can be formulated using Eq. (7):

$$\mathbf{A} = \begin{bmatrix} 0 & 1 & 0 & 0 & 0 & 0 \\ -266.7 & -1.2 & 300 & 0.8603 & 0 & 0 \\ 0 & 0 & 0 & 1 & 0 & 0 \\ 266.7 & 0.7647 & -600 & -2.156 & 266.7 & 0.7647 \\ 0 & 0 & 0 & 0 & 0 & 1 \\ 0 & 0 & 300 & 0.8603 & -533.3 & -1.965 \end{bmatrix}, \quad \mathbf{B} = \begin{bmatrix} 0 & 0 & 0 \\ -1.667 & 1.667 & 0 \\ 0 & 0 & 0 \\ 1.667 & -3.333 & 1.667 \\ 0 & 0 & 0 \\ 0 & 1.667 & -3.333 \end{bmatrix} \times 10^{-4}, \quad \mathbf{E} = \begin{bmatrix} 0 \\ -1 \\ 0 \\ 0 \\ 0 \\ 0 \end{bmatrix} \tag{31}$$

Note that the state-space vector corresponding to these matrices no longer contains displacements and velocities relative to the ground. Instead, the vector has been formulated to contain inter-story drifts and velocities that are grouped by floors, as shown in Eq. (5). The above matrices in the continuous-time domain can be converted into their discrete-time equivalents for a given sampling frequency. For the results presented here, a sampling frequency of 100 Hz is employed. The output matrices $\mathbf{C_z}$ and $\mathbf{D_z}$ in Eq. (23) are defined as:

$$\mathbf{C_z} = \left[\begin{array}{cccccc} 50 & 0 & 0 & 0 & 0 & 0 \\ 0 & 0 & 50 & 0 & 0 & 0 \\ 0 & 0 & 0 & 0 & 50 & 0 \\ \hline 0 & 0 & 0 & 0 & 0 & 0 \\ 0 & 0 & 0 & 0 & 0 & 0 \\ 0 & 0 & 0 & 0 & 0 & 0 \end{array}\right], \quad \mathbf{D_z} = \left[\begin{array}{ccc} 0 & 0 & 0 \\ 0 & 0 & 0 \\ 0 & 0 & 0 \\ \hline 3.162 & 0 & 0 \\ 0 & 3.162 & 0 \\ 0 & 0 & 3.162 \end{array}\right] \times 10^{-5} \tag{32}$$

The above assignments for $\mathbf{C_z}$ and $\mathbf{D_z}$ make the 2-norm of the output vector $\mathbf{z_d}[k]$ a quadratic function of the inter-story drifts and control forces:

$$
\begin{aligned}
\left\|\mathbf{z_d}[k]\right\|_2^2 &= \left\|\left(\mathbf{C_z}+\mathbf{D_z}\mathbf{G_d}\right)\mathbf{x_d}[k]\right\|_2^2 \\
&= \left\|\mathbf{C_z}\mathbf{x_d}[k]+\mathbf{D_z}\mathbf{u_d}[k]\right\|_2^2 \\
&= 2500\left[q_1^2[k]+\left(q_2[k]-q_1[k]\right)^2+\left(q_3[k]-q_2[k]\right)^2\right] \\
&\quad +10^{-9}\left(u_1^2[k]+u_2^2[k]+u_3^2[k]\right)
\end{aligned}
\tag{33}
$$

Using the system matrices defined above in Eqs. (31) and (32), the convex optimization problem in Eq. (28) can be solved according to different sparsity requirements imposed on the $\mathbf{Y_d}$ and $\mathbf{\Theta_d}$ matrices. In this example, sparsity patterns *I* and *II* defined in Eq. (20) and (21) are first employed. For these two patterns, solutions to the optimization problem result in the following decentralized control gain matrices, respectively:

$$
\mathbf{G}_{\mathbf{d}I}=\begin{bmatrix} -1.578 & 5.608 & & & & \\ & & -5.383 & 3.195 & & \\ & & & & -4.109 & 3.013 \end{bmatrix}\times 10^5 \tag{34}
$$

$$
\mathbf{G}_{\mathbf{d}II}=\begin{bmatrix} -4.246 & 10.12 & 10.59 & 11.86 & & \\ 4.747 & 4.141 & -7.363 & 11.77 & -0.1178 & -0.0788 \\ & & 5.106 & 6.320 & -9.763 & 4.061 \end{bmatrix}\times 10^5 \tag{35}
$$

When no sparsity pattern is applied to $\mathbf{Y_d}$ and $\mathbf{\Theta_d}$, a full gain matrix representing centralized feedback is generated:

$$
\mathbf{G}_{III}=\begin{bmatrix} 2.354 & 15.24 & -0.6553 & 11.52 & 1.505 & 6.281 \\ -3.719 & 10.04 & 3.358 & 8.539 & 1.125 & 4.499 \\ -3.954 & 5.742 & -1.599 & 4.726 & 5.687 & 3.269 \end{bmatrix}\times 10^5 \tag{36}
$$

The open-loop $\mathcal{H}_\infty$-norm of the uncontrolled structure and the closed-loop $\mathcal{H}_\infty$-norms of the controlled structure using the above gain matrices are listed in Table 1. The $\mathcal{H}_\infty$-norm of the uncontrolled structure is computed using the discrete-time system defined in Eq. (22) with the gain matrix $\mathbf{G_d}$ set as a zero matrix. Comparing the four cases presented herein, the uncontrolled structure has the highest $\mathcal{H}_\infty$-norm (8.4366), which indicates the largest "worst-case" amplification from the excitation input $\mathbf{w_d}$ to the output $\mathbf{z_d}$. Among the three controlled cases, because the centralized case with gain matrix $\mathbf{G}_{\mathbf{d}III}$ assumes that complete state information is available for control decisions, the lowest $\mathcal{H}_\infty$-norm (0.7045) is

Table 1. $\mathcal{H}_2$ and $\mathcal{H}_\infty$-norms of the open-loop transfer function $\mathbf{H_{zw}}$ and the closed-loop norms using both the $\mathcal{H}_\infty$ controllers and LQR controllers

	Open-loop (Uncontrolled)	Closed-loop					
		Fully decentralized		Partially decentralized		Centralized	
		$\mathbf{G}_{\mathbf{d}I}^{\mathrm{LQR}}$	$\mathbf{G}_{\mathbf{d}I}$ ($\mathcal{H}_\infty$)	$\mathbf{G}_{\mathbf{d}II}^{\mathrm{LQR}}$	$\mathbf{G}_{\mathbf{d}II}$ ($\mathcal{H}_\infty$)	$\mathbf{G}_{\mathbf{d}III}^{\mathrm{LQR}}$	$\mathbf{G}_{\mathbf{d}III}$ ($\mathcal{H}_\infty$)
$\mathcal{H}_\infty$ norm	8.4366	1.2836	0.8521	1.0462	0.7076	0.9922	0.7045
$\mathcal{H}_2$ norm	0.4657	0.1874	0.3020	0.1786	0.5027	0.1772	0.6108

achieved (which means best control performance). The fully decentralized case with gain matrix $\mathbf{G}_{\mathbf{d}I}$ has the largest norm (0.8521) among the three $\mathcal{H}_\infty$ controllers; this is expected because the fully decentralized controller has the least amount of information available for calculating control decisions for each control device.

The 1940 El Centro NS (Imperial Valley Irrigation District Station) earthquake record with its peak acceleration scaled to 1m/s^2 is used as the ground excitation. Three ideal actuators that generate any desired control force are deployed at the three stories. Maximum inter-story drifts and control forces during the dynamic response are plotted in Figure 2. The inter-story drift plots in Figure 2(a) include the results for the uncontrolled structure and the structure controlled using the three different gain matrices. Using ideal actuators, all three controlled cases achieve significant reduction in inter-story drifts compared with the uncontrolled case. Among the three controlled cases, the fully decentralized case using gain matrix $\mathbf{G}_{\mathbf{d}I}$ achieves the smallest reduction in inter-story drifts, which is consistent with the performance comparison indicated by the $\mathcal{H}_\infty$-norms in Table 1. The difference between the cases using gain matrices $\mathbf{G}_{\mathbf{d}II}$ and $\mathbf{G}_{\mathbf{d}III}$ is minor, with $\mathbf{G}_{\mathbf{d}III}$ achieving slightly better performance. Figure 2(b) presents the peak control forces for the three controlled cases. The fully decentralized controller imposes the lowest requirements on the control force capacity. The peak control forces are similar between the partially decentralized case $\mathbf{G}_{\mathbf{d}II}$ and the centralized case $\mathbf{G}_{\mathbf{d}III}$.

3.1.2. Comparison with decentralized LQR control

It could be instructive to compare the decentralized $\mathcal{H}_\infty$ controller design with the decentralized LQR controller design that was previously studied [10]. The LQR control algorithm aims to select the optimal control force trajectory $\mathbf{u_d}$ by minimizing the expected value of a quadratic cost function, J :

$$J = \sum_{k=1}^{K} \left(\mathbf{x_d}^{\mathrm{T}}[k]\mathbf{Q}\mathbf{x_d}[k] + \mathbf{u_d}^{\mathrm{T}}[k]\mathbf{R}\mathbf{u_d}[k] \right),\ \mathbf{Q}_{2n\times 2n} \geq 0 \text{ and } \mathbf{R}_{m_2\times m_2} > 0 \qquad (37)$$

Using the same definition of the output matrices as described in Eq. (32), the following weighting matrices are employed for the LQR controller design:

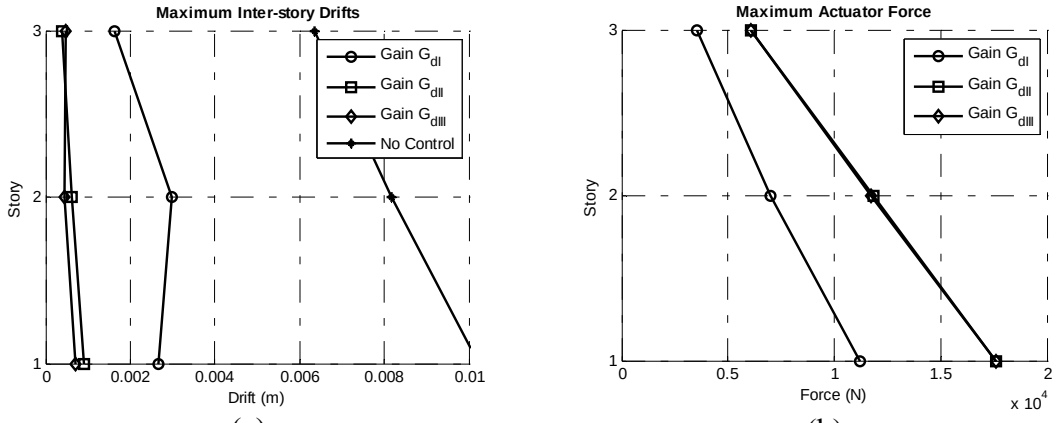

Figure 2. Simulation results when ideal actuators are deployed on the 3-story structure.

$$\mathbf{Q} = \mathbf{C_z}^{\mathrm{T}}\mathbf{C_z} \tag{38}$$

$$\mathbf{R} = \mathbf{D_z}^{\mathrm{T}}\mathbf{D_z} \tag{39}$$

As a result, the LQR optimization index J is proportional to the signal 2-norm of the system output:

$$\begin{aligned} J &= \sum_{k=1}^{K}\left(\mathbf{x_d}^{\mathrm{T}}[k]\mathbf{C_z}^{\mathrm{T}}\mathbf{C_z}\mathbf{x_d}[k] + \mathbf{u_d}^{\mathrm{T}}[k]\mathbf{D_z}^{\mathrm{T}}\mathbf{D_z}\mathbf{u_d}[k]\right) \\ &= \sum_{k=1}^{K}\left\|\mathbf{C_z}\mathbf{x_d}[k] + \mathbf{D_z}\mathbf{u_d}[k]\right\|_2^2 \\ &= \sum_{k=1}^{K}\left\|\mathbf{z_d}[k]\right\|_2^2 \\ &= \left\|\mathbf{z_d}\right\|_2^2 / \Delta t \end{aligned} \tag{40}$$

where Δt is the sampling period, and note that $\mathbf{C_z}^{\mathrm{T}}\mathbf{D_z} = \mathbf{0}$ and $\mathbf{D_z}^{\mathrm{T}}\mathbf{C_z} = \mathbf{0}$ using the definitions in Eq. (32). The design of the LQR controller iteratively searches for an optimal control gain matrix by traversing along the optimization gradient. Sparsity shape constraints are iteratively applied to the search gradient in order to compute decentralized gain matrices. As a result, the following three decentralized/centralized LQR gain matrices can be computed:

$$\mathbf{G}_{\mathbf{d}I}^{\mathrm{LQR}} = \begin{bmatrix} 4.4137 & 1.2649 & & & & \\ & & 4.6383 & 0.9489 & & \\ & & & & 5.1068 & 0.6965 \end{bmatrix} \times 10^5 \tag{41}$$

$$\mathbf{G}_{\mathbf{d}II}^{\mathrm{LQR}} = \begin{bmatrix} 5.4594 & 1.2150 & -0.3170 & 0.4404 & & \\ 0.5689 & 0.5262 & 4.0575 & 0.8687 & 0.2693 & 0.2932 \\ & & -0.1671 & 0.2163 & 5.0089 & 0.6818 \end{bmatrix} \times 10^5 \tag{42}$$

$$\mathbf{G}_{\mathbf{d}III}^{\mathrm{LQR}} = \begin{bmatrix} 5.2399 & 1.2321 & 0.8256 & 0.5676 & 0.1599 & 0.2438 \\ 0.5157 & 0.5230 & 4.1441 & 0.8631 & 0.4141 & 0.2975 \\ 0.1322 & 0.2427 & 0.6449 & 0.3228 & 4.5696 & 0.6714 \end{bmatrix} \times 10^5 \tag{43}$$

Table 1 also lists the $\mathcal{H}_2$ and $\mathcal{H}_\infty$-norms of the open-loop transfer function $\mathbf{H_{zw}}$ and the closed-loop norms using both the $\mathcal{H}_\infty$ controllers and the LQR controllers. Since the LQR control approach is equivalent to an $\mathcal{H}_2$ control design that minimizes the closed-loop $\mathcal{H}_2$-norm, LQR controllers are expected to perform well in reducing the closed-loop $\mathcal{H}_2$-norm [12; 28]. Similar to the $\mathcal{H}_\infty$ norm, definition of the system $\mathcal{H}_2$-norm can also be written in terms of the singular values of the transfer function matrix:

$$\left\|\mathbf{H_{zw}}(s)\right\|_2 = \sqrt{\frac{1}{2\pi}\int_{-\infty}^{+\infty}\sum_i \sigma_i^2\left[\mathbf{H_{zw}}(\mathrm{j}\omega)\right]d\omega} \tag{44}$$

As expected, Table 1 shows that the LQR controllers, no matter decentralized or centralized, consistently perform better than their $\mathcal{H}_\infty$ counterparts in reducing the $\mathcal{H}_2$-norm, while the $\mathcal{H}_\infty$ controllers consistently perform better than their LQR counterparts in terms of reducing the $\mathcal{H}_\infty$-norm.

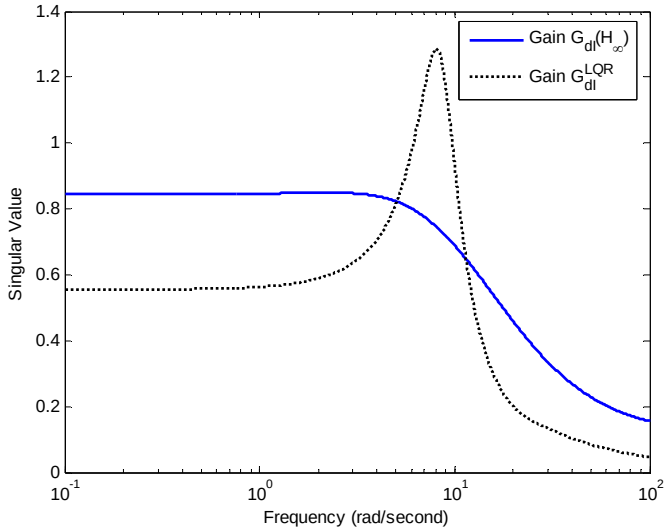

Figure 3. Singular values of the closed-loop system transfer function $\mathbf{H}_{\mathbf{zw}}(j\omega)$ using the decentralized $\mathcal{H}_\infty$ controller $\mathbf{G}_{\mathbf{d}I}$ and decentralized LQR controller $\mathbf{G}_{\mathbf{d}I}^{\mathrm{LQR}}$

In this example, the second dimension of the transfer function matrix $\mathbf{H}_{\mathbf{zw}}(j\omega)$ is one, because the disturbance **w** is a scalar that represents the ground excitation. Therefore, $\mathbf{H}_{\mathbf{zw}}(j\omega)$ has only one singular value at each frequency ω, which is the largest singular value. Figure 3 plots the singular value of the closed-loop system transfer function $\mathbf{H}_{\mathbf{zw}}(j\omega)$ using the decentralized $\mathcal{H}_\infty$ controller $\mathbf{G}_{\mathbf{d}I}$ and the decentralized LQR controller $\mathbf{G}_{\mathbf{d}I}^{\mathrm{LQR}}$. The definition of the system $\mathcal{H}_\infty$ norm in Eq. (12) shows that the $\mathcal{H}_\infty$ norm should be equal to the peak of the largest singular value over the frequency span. Correspondingly, Figure 3 shows that the peak of the singular value using the $\mathcal{H}_\infty$ controller $\mathbf{G}_{\mathbf{d}I}$ is 0.85, while the peak for the LQR controller $\mathbf{G}_{\mathbf{d}I}^{\mathrm{LQR}}$ is 1.28; both of which are consistent with the $\mathcal{H}_\infty$ norms listed in Table 1. Figure 3 also illustrates that the decentralized $\mathcal{H}_\infty$ controller excels at "pushing down the peak of the largest singular value". In comparison, the decentralized LQR controller is shown to excel in reducing all singular values over the entire frequency span, which agrees with the objective of minimizing the $\mathcal{H}_2$ norm (as defined in Eq. (44)).

Simulations are conducted using the LQR controllers, with the same 1940 El Centro NS earthquake excitation scaled to 1m/s^2. Three ideal actuators are again deployed at the three stories. Maximum inter-story drifts and control forces during the dynamic response are plotted in Figure 4. Comparison between Figure 4 and Figure 2 shows that LQR controllers generally achieve less reduction to peak inter-story drifts. On the other hand, the advantage of the LQR controllers in this example is that they impose lower requirements to the force capacity of the structural control devices.

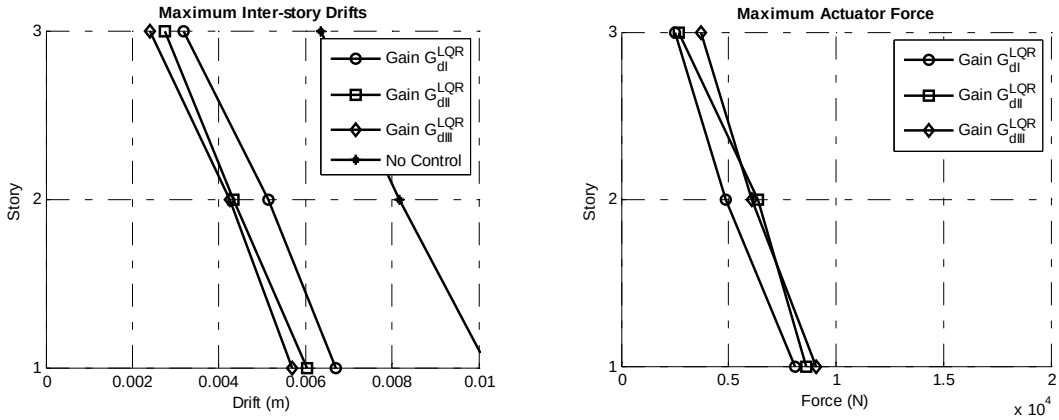

(a) (b)

Figure 4. Simulation results when ideal actuators are deployed on the 3-story structure.

3.2. Numerical simulation of a 20-story benchmark structure

3.2.1. Simulation using ideal actuators

To explore the performance of decentralized $\mathcal{H}_\infty$ control for a larger-scale structure, a 20-story benchmark building designed for the Structural Engineers Association of California (SAC) project is selected [29]. Same as the 3-story example, discrete-time controllers are adopted in the simulation. The building is modeled as an in-plane lumped-mass shear structure with control devices allocated between every set of neighboring floors. Figure 5(a) shows the mass, stiffness, and damping parameters of the structure. In the numerical simulations, it is assumed that both the inter-story drifts and inter-story velocities between every two neighboring floors are measurable. As shown in Eq. (5), the state-space equations are formulated such that the state-space vector contains inter-story drifts and velocities. Simulations are conducted for different decentralization schemes as shown in Figure 5(b). The degree-of-centralization (DC) reflects the different communication architectures, with each communication subnet (as denoted by channels Ch1, Ch2, etc.) covering a limited number of stories. The control devices covered by a subnet are allowed

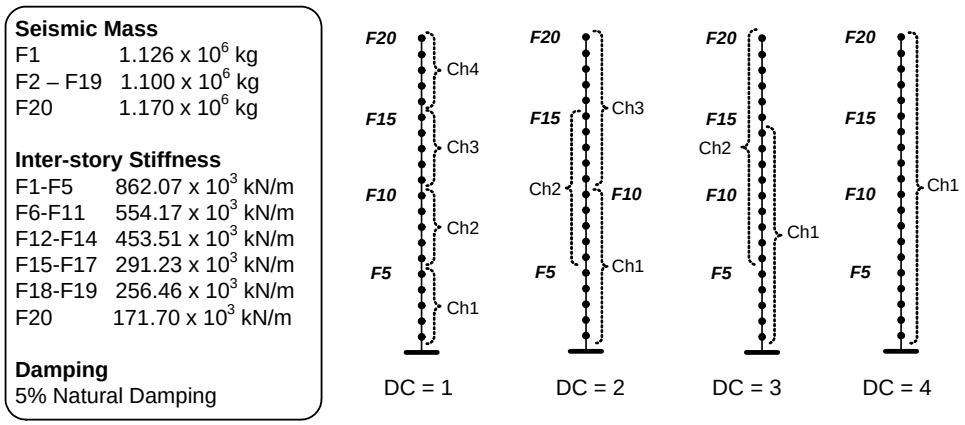

(a) (b)

Figure 5. Twenty-story SAC building for numerical simulations: (a) model parameters of the lumped mass structure; (b) communication subnet partitioning for different degrees-of-centralization (DC).

to access the sensor data within that subnet. For example, the case where DC = 1 has each subnet covering only five stories with a total of four subnets utilized. For DC = 2, each subnet covers ten stories and a total of three subnets are utilized; meanwhile, overlaps exist between subnets for DC = 2. The gain matrices for these two decentralized information structures have following sparsity patterns:

$$\mathbf{G_d} = \text{ 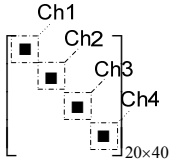 } \text{ when DC} = 1 \quad \mathbf{G_d} = \text{ 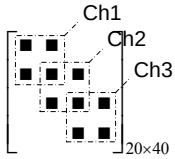 } \text{ when DC} = 2 \tag{45}$$

Each entry in the above matrices represents a 5 × 10 block submatrix. To achieve the sparsity patterns in gain matrix $\mathbf{G_d}$, the matrix variable $\mathbf{Y_d}$ in Eq. (28) is defined to have the same sparsity pattern as $\mathbf{G_d}$, and $\mathbf{\Theta_d}$ is defined to be always block-diagonal. For the cases where DC = 3 and DC = 4, the number of stories covered by each communication subnet increases accordingly, which result in fewer zero blocks in $\mathbf{G_d}$. Clearly, the case where DC = 4 corresponds to a centralized feedback structure with all devices in the same subnet (*i.e.* Ch 1).

To investigate the effectiveness of the proposed decentralized control design, we first assume the 20-story structure is instrumented with ideal actuators that can produce any desired force. Output matrices $\mathbf{C_z}$ and $\mathbf{D_z}$ in Eq. (23) are defined as:

$$\mathbf{C_z} = \begin{bmatrix} 10^2 \mathbf{I}_{40\times 40} \\ \mathbf{0}_{20\times 40} \end{bmatrix}, \ \mathbf{D_z} = \begin{bmatrix} \mathbf{0}_{40\times 20} \\ 10^{-12} \mathbf{I}_{20\times 20} \end{bmatrix} \tag{46}$$

Simulations are performed for different degrees-of-centralization (DC = 1,…,4) and sampling periods (ranging from 0.01 s to 0.06 s at a resolution of 0.01 s). Additionally, three ground motion records all scaled to a peak ground acceleration (PGA) of 1 m/s^2 are used for the simulation: 1940 El Centro NS (Imperial Valley Irrigation District Station), 1995 Kobe NS (JMA Station), and 1999 Chi-Chi NS (TCU-076 Station). Two representative performance indices, J_1 and J_2, as proposed by Spencer, *et al*. [29] are adopted:

$$J_1 = \max_{\text{Earthquakes}} \left\{ \max_{k,i} d_i[k] \Big/ \max_{k,i} \hat{d}_i[k] \right\} \tag{47}$$

$$J_2 = \max_{\text{Earthquakes}} \left\{ \|\mathbf{z_d}\|_2^2 \Big/ \|\hat{\mathbf{z}}_\mathbf{d}\|_2^2 \right\} \tag{48}$$

Here J_1 and J_2 correspond to maximum inter-story drifts and output vector $\mathbf{z_d}$, respectively. In Eq. (47), $d_i[k]$ represents the inter-story drift between floor i (i = 1, …, n) and its lower floor at time step k, and $\max_{k,i} d_i[k]$ is the maximum inter-story drift over the entire time history and among all floors. The maximum inter-story drift is normalized by its counterpart $\max_{k,i} \hat{d}_i[k]$, which is the maximum response of the uncontrolled structure. The largest normalized ratio among the simulations for the three different earthquake records is defined as the performance index J_1. Similarly, the performance index J_2 is defined in Eq.

(48) based on the 2-norm of the output vector $\mathbf{z_d}$; *i.e.* $\|\mathbf{z_d}\|_2^2 = \Delta t \sum_{k=1}^{K} \mathbf{z_d}^{\mathrm{T}}[k]\mathbf{z_d}[k]$, with K being the last time step of the simulation. When computing the two indices, a uniform sampling period of 0.001 s is used to collect the structural response data points for $d_i[k]$ and $\mathbf{z_d}[k]$, regardless of the sampling period of the feedback control scheme. Because these indices have been normalized against the performance of the uncontrolled structure, values less than one indicate that the closed-loop control solution is effective with smaller index values indicating better overall control performance.

Figure 6 shows the control performance indices for different degrees-of-centralization and sampling rates. Generally speaking, control performance is better for higher degrees-of-centralization and shorter sampling periods. The plots show that all control schemes achieve obvious reduction in structural response when compared to the uncontrolled case, *i.e.* the normalized performance indices are much less than one. To better review the simulation results, the performance indices for the four different control schemes are re-plotted as a function of sampling period in Figure 6(c) and (d). Figure 6(d) clearly illustrates the expected comparison among the four control cases, *i.e.* for each sampling time, the achieved output norm generally decreases as the degree of centralization increases.

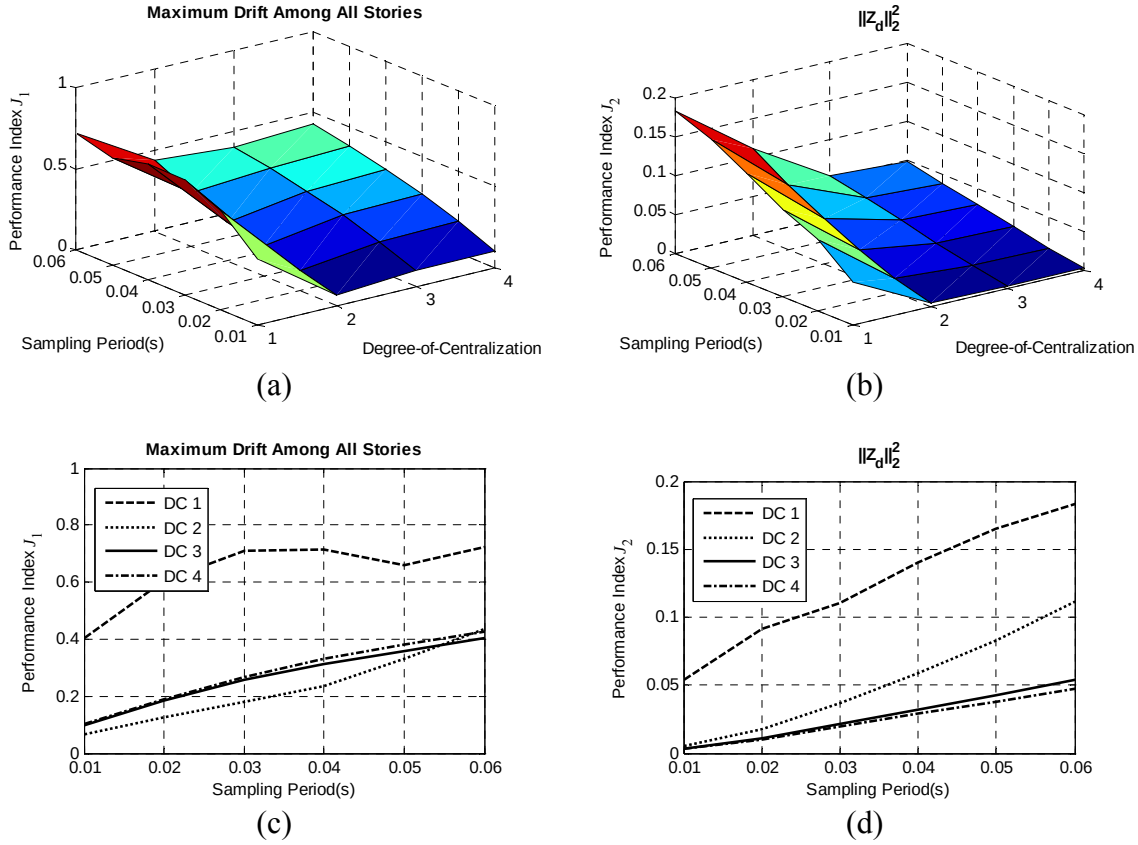

Figure 6. Simulation results for the 20-story SAC building instrumented with ideal actuators. The plots illustrate performance indices for different sampling steps and degrees-of-centralization (DC): (a) 3D plot for performance index J_1; (b) 3D plot for performance index J_2; (c) condensed 2D plot for J_1; (d) condensed 2D plot for J_2.

While it may appear from Figure 6 that a centralized control architecture always performs better than decentralized ones operating at the same sampling frequency, such a centralized system with high nodal counts might be economically and technically difficult to implement in large-scale civil structures. For example, significant communication and computation resources are usually required to implement a large-scale centralized control system. As a result, longer sampling periods need to be adopted, which in turn, reduces the effectiveness of the centralized solution. In contrast, if a decentralized architecture is implemented, the control system would be capable of shorter sampling periods that lead to potential improvement in the control performance. It can be observed from Figure 6 that if shorter sampling periods are adopted in partially decentralized control systems (DC2 or DC3), smaller performance indices can be achieved when compared with a centralized system (DC4) that adopts a longer sampling period. The trade-off between centralization and sampling period will be further explored in the next simulation analysis.

3.2.2. Simulation using semi-active hydraulic dampers (SHD)

To investigate the performance of decentralized $\mathcal{H}_\infty$ control using realistic structural control devices, semi-active hydraulic dampers (SHD) are employed in further simulations for the 20-story structure. The arrangement of SHD dampers in the building is shown in Figure 7(a). From lower to higher floors, the number of instrumented SHD dampers decreases gradually from 4 to 1. Figure 7(b) shows the installation of a SHD damper between two floors using a V-brace, together with key parameters of the damper. To accurately model the damping force, the Maxwell element proposed by Hatada, *et al*. [30] is employed. In a Maxwell element, a dashpot and a stiffness spring are connected in series, which result in a damping force described by the following differential equation:

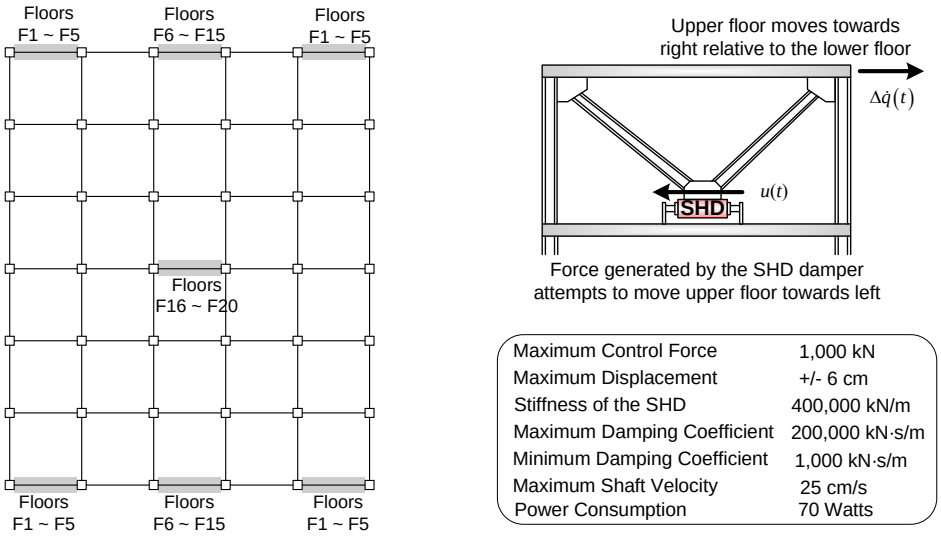

Figure 7. Instrumentation of semi-active hydraulic dampers (SHD) in the 20-story structure: (a) layout of dampers on the floor plans; (b) key parameters of the dampers.

$$\dot{u}(t) + \frac{k_{eff}}{c_{SHD}(t)} u(t) = k_{eff} \Delta\dot{q}(t) \tag{49}$$

where $u(t)$ and $\Delta\dot{q}(t)$ denote the damping force and the inter-story velocity, respectively, k_{eff} represents the effective stiffness of the damper in series with the V-brace, and $c_{SHD}(t)$ is the adjustable damping coefficient of the SHD damper.

When the SHD damper is deployed in a feedback control system, if the desired damping force $u(t)$ is in an opposite direction to the inter-story velocity $\Delta\dot{q}(t)$, as shown in Figure 7(b), the damping coefficient $c_{SHD}(t)$ is adjusted so that the damper generates a force closest to the desired force. If the desired force is in the same direction to the inter-story velocity, the damping coefficient is set to its minimum value at 1,000 kN·s/m.

An important criterion to consider in evaluating a feedback control system, whether being centralized or decentralized, is that the feedback control system should perform better than a passive control system. When the SHD dampers are employed, fixing the damping coefficients of all dampers at either minimum (1,000 kN·s/m) or maximum (200,000 kN·s/m) values constitutes a passive control system. Figure 8 presents the simulated maximum inter-story drifts when the structure is excited using the three ground motions with the PGA (peak ground acceleration) scaled to 1m/s^2: 1940 El Centro NS, 1995 Kobe NS, and 1999 Chi-Chi NS. Four cases are plotted for each earthquake: the case without control, the passive case with minimum damping, the passive case with maximum damping, and a decentralized semi-active control case. For the decentralized semi-active control case, the DC (degrees-of-centralization) is 2 (Figure 5) and the sampling frequency

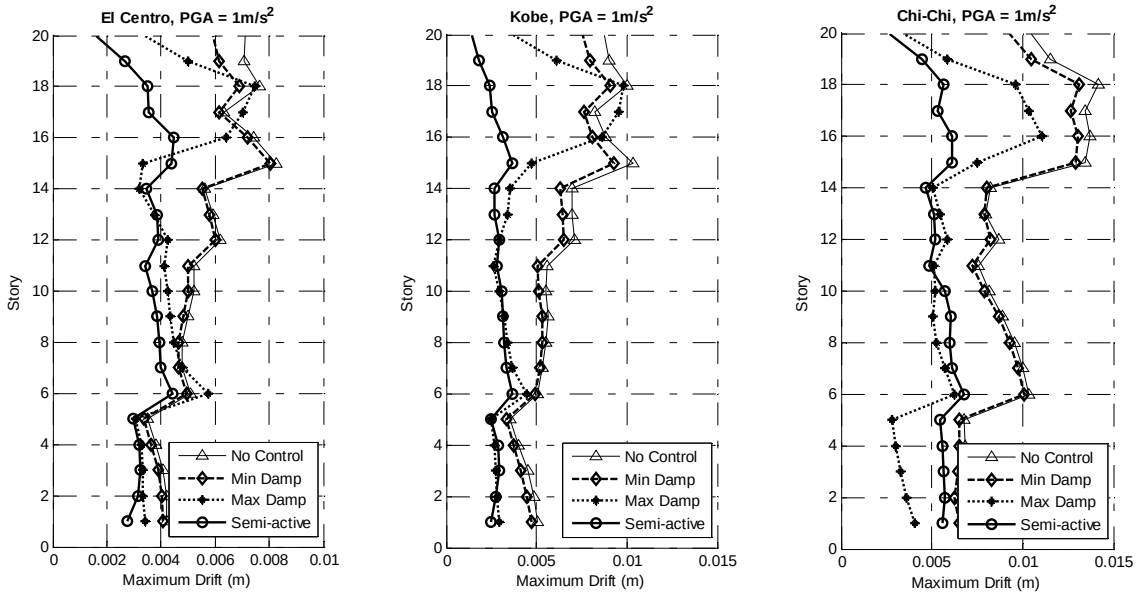

Figure 8. Maximum inter-story drifts for cases without control, with passive control (damping coefficients of all SHD dampers fixed at minimum or maximum), and with decentralized semi-active control (DC = 2 and 100 Hz sampling frequency).

is 100 Hz. It is found that the decentralized $\mathcal{H}_\infty$ controller with the following output matrices, $\mathbf{C_z}$ and $\mathbf{D_z}$:

$$\mathbf{C_z} = \begin{bmatrix} 10^5 \mathbf{I}_{40\times 40} \\ \mathbf{0}_{20\times 40} \end{bmatrix}, \ \mathbf{D_z} = \begin{bmatrix} \mathbf{0}_{40\times 20} \\ 10^{-5.5} \mathbf{I}_{20\times 20} \end{bmatrix} \tag{50}$$

achieves satisfactory results. As shown in Figure 8, all three control schemes, including two passive and one semi-active, reduce the maximum inter-story drifts compared with the uncontrolled case. The passive control case with maximum damping generally results in less inter-story drifts than the passive case with minimum damping, except at a few higher floors for the El Centro and Kobe earthquakes. Meanwhile, the decentralized semi-active control case not only effectively reduces drifts at lower floors, but also achieves greater mitigation of drifts at the higher floors compared to the two passive cases. Better performance of the decentralized semi-active control case is observed for all three earthquake records. For the Kobe earthquake, decentralized semi-active control reduces the drift at the 18th story by about 75% compared with the uncontrolled and the two passive control cases. This shows that in the passive case with maximum damping, dampers at each story may only attempt to reduce local responses and results in conflict among damper efforts at different stories. While in the semi-active control case that aims to minimize the overall $\mathcal{H}_\infty$ norm of the global structural system, efforts from dampers at different stories can be better coordinated to reduce overall structural response.

Figure 9 compares the performance indices for the 20-story structure instrumented with semi-active hydraulic dampers, when different control schemes are adopted. The two passive control schemes include the maximum and minimum damping cases. To illustrate the effect of faster sampling frequency (*i.e.* shorter sampling periods) in decentralized feedback control, feedback control cases with different centralization degrees (DC = 1,…,4) are associated with different sampling frequencies. For each centralization degree, the sampling frequency is selected in reverse proportion to the number of stories contained in one communication subnet (shown in Figure 5). For example, a sampling frequency of 100 Hz is associated with case DC2, while a sampling frequency of 50 Hz is associated with the centralized case DC4 due to larger communication and computation burdens. The same three ground motion records scaled to a peak acceleration of 1 m/s^2 are used in the simulation: 1940 El Centro NS, 1995 Kobe NS (JMA Station), and 1999 Chi-Chi. As shown in Figure 9, the feedback control cases generally achieve better performance when compared with two passive control cases. Furthermore, the figure illustrates that although decentralized feedback control cases do not have complete sensor data available while calculating control decisions, they may outperform the centralized case due to the faster sampling frequencies that are available through decentralization. For example, compared with the centralized scheme DC4 (at 50Hz), the partially decentralized scheme DC2 (at 100Hz) can provide larger reduction to both maximum inter-story drift and the 2-norm of the output vector $\mathbf{z_d}$.

4. SUMMARY AND CONCLUSION

This paper presents pilot studies in exploring decentralized structural control design that minimizes the closed-loop $\mathcal{H}_\infty$ norm. The decentralized control design offers promising

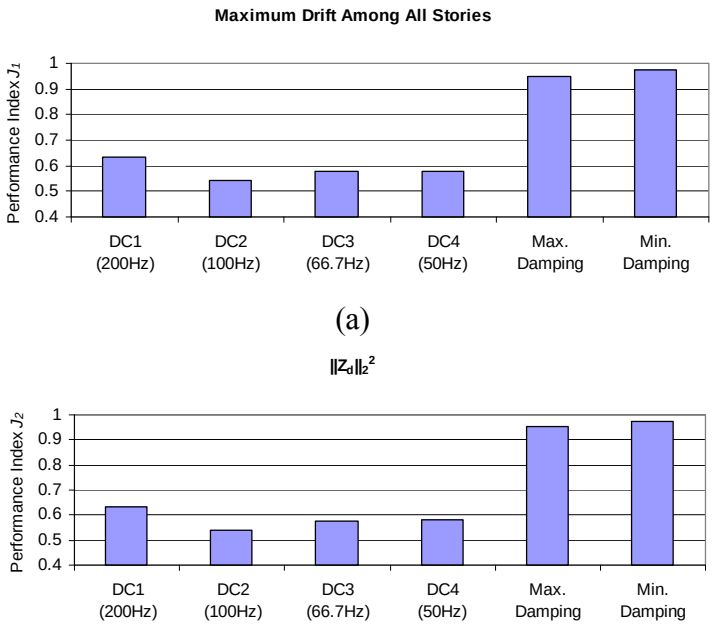

Figure 9. Simulation results for the 20-story SAC building instrumented with semi-active hydraulic dampers (SHD). The plots illustrate performance indices for passive control cases and semi-active feedback control cases with different degrees-of-centralization (DC) and sampling frequencies: (a) performance index J_1; (b) performance index J_2.

solutions to large-scale structural sensing and control systems. Solutions are developed for both continuous-time and discrete-time formulations. The properties of linear matrix inequalities are utilized to convert the complicated decentralized $\mathcal{H}_\infty$ control problem into a simple convex optimization problem. Once proposed as a convex optimization problem, decentralized architectures are easily imposed to yield decentralized $\mathcal{H}_\infty$ control solutions. Such solutions are necessary to provide control systems with the ability to scale with number of sensors and actuators implemented in the system.

Numerical simulation results using a 3-story and a 20-story structure illustrate the feasibility of the different decentralized control architectures. Comparison between the performance of the decentralized $\mathcal{H}_\infty$ controllers and the performance of decentralized LQR-based controllers illustrates that the controllers both deliver expected performance. The simulation results also demonstrate that when realistic semi-active control devices (such as the SHD dampers) are used in combination with the decentralized $\mathcal{H}_\infty$ control algorithm, better performance can be gained over the passive control cases. It is also illustrated that decentralized control strategies may provide equivalent or even superior control performance, given that their centralized counterparts could suffer longer sampling periods due to communication and computation constraints.

Drawbacks of the presented decentralized $\mathcal{H}_\infty$ control design include the inability to consider the effect of time delay in the feedback loop and the requirement for inter-story

drift and velocity data for feedback. Future research in decentralized $\mathcal{H}_\infty$ control may consider time delay effects in the control algorithm and utilize system output feedback. Furthermore, dynamic output feedback will be explored instead of static feedback, to capitalize on a much larger controller parametric space. Comparative studies will then be conducted between the decentralized $\mathcal{H}_\infty$ control design and the previously proposed decentralized control design which is based on LQR (linear quadratic regulator) criteria and considers time delay effects [10].

5. ACKNOWLEDGEMENT

This research is partially funded by the Office of Naval Research through the Young Investigator Award received by Prof. Jerome P. Lynch at the University of Michigan. Part of the research was accomplished during Prof. Yang Wang's Ph.D. study at Stanford University, where he was supported by the Office of Technology Licensing Stanford Graduate Fellowship. The authors would like to thank Prof. Chin-Hsiung Loh at the National Taiwan University for sharing the numerical model of the 3-story structure, which is based on an experimental structure built at the National Center for Research on Earthquake Engineering in Taiwan.

REFERENCES

[1] Soong TT. *Active Structural Control: Theory and Practice.* Wiley: Harlow, Essex, England, 1990.

[2] Spencer BF, Jr. and Nagarajaiah S. State of the art of structural control. *Journal of Structural Engineering* 2003; **129** (7): 845-856.

[3] Yao JTP. Concept of structural control. *Journal of Structural Division, ASCE* 1972; **98** (7): 1567-1574.

[4] Housner GW, Bergman LA, Caughey TK, Chassiakos AG, Claus RO, Masri SF, Skelton RE, Soong TT, Spencer BF, Jr. and Yao JTP. Structural control: past, present, and future. *Journal of Engineering Mechanics* 1997; **123** (9): 897-971.

[5] Chu SY, Soong TT and Reinhorn AM. Active, Hybrid, and Semi-active Structural Control: a Design and Implementation Handbook. Wiley: Hoboken, NJ, 2005.

[6] Sandell N, Jr., Varaiya P, Athans M and Safonov M. Survey of decentralized control methods for large scale systems. *Automatic Control, IEEE Transactions on* 1978; **23** (2): 108-128.

[7] Siljak DD. *Decentralized Control of Complex Systems.* Academic Press: Boston, 1991.

[8] Lunze J. *Feedback Control of Large Scale Systems.* Prentice-Hall: Englewood Cliffs, NJ, 1992.

[9] Shimizu K, Yamada T, Tagami J and Kurino H. Vibration tests of actual buildings with semi-active switching oil damper. *Proceedings of the 13th World Conference on Earthquake Engineering*. Vancouver, B.C., Canada, August 1 - 6, 2004.

[10] Wang Y, Swartz RA, Lynch JP, Law KH, Lu K-C and Loh C-H. Decentralized civil structural control using real-time wireless sensing and embedded computing. *Smart Structures and Systems* 2007; **3** (3): 321-340.

[11] Wang Y. *Wireless Sensing and Decentralized Control for Civil Structures: Theory and Implementation*. PhD Thesis, Department of Civil and Environmental Engineering, Stanford University, Stanford, CA, 2007.

[12] Skogestad S and Postlethwaite I. *Multivariable Feedback Control: Analysis and Design.* John Wiley: Chichester, West Sussex, England, 2005.
[13] Balandin DV and Kogan MM. LMI-based optimal attenuation of multi-storey building oscillations under seismic excitations. *Structural Control and Health Monitoring* 2005; **12** (2): 213-224.
[14] Chase JG and Smith HA. Robust H_∞ control considering actuator saturation. I: theory. *Journal of Engineering Mechanics* 1996; **122** (10): 976-983.
[15] Jabbari F, Schmitendorf WE and Yang JN. H_∞ control for seismic-excited buildings with acceleration feedback. *Journal of Engineering Mechanics* 1995; **121** (9): 994-1002.
[16] Lin C-C, Chang C-C and Chen H-L. Optimal H_∞ output feedback control systems with time delay. *Journal of Engineering Mechanics* 2006; **132** (10): 1096-1105.
[17] Mahmoud MS, Terro MJ and Abdel-Rohman M. An LMI approach to H_∞-control of time-delay systems for the benchmark problem. *Earthquake Engineering & Structural Dynamics* 1998; **27** (9): 957-976.
[18] Johnson EA, Voulgaris PG and Bergman LA. Multiobjective optimal structural control of the Notre Dame building model benchmark. *Earthquake Engineering & Structural Dynamics* 1998; **27** (11): 1165-1187.
[19] Narasimhan S and Nagarajaiah S. Smart base isolated buildings with variable friction systems: H_∞ controller and SAIVF device. *Earthquake Engineering & Structural Dynamics* 2006; **35** (8): 921-942.
[20] Yang JN, Lin S and Jabbari F. H_∞-based control strategies for civil engineering structures. *Structural Control and Health Monitoring* 2004; **11** (3): 223-237.
[21] Wang S-G. Robust active control for uncertain structural systems with acceleration sensors. *Journal of Structural Control* 2003; **10** (1): 59-76.
[22] Boyd SP, El Ghaoui L, Feron E and Balakrishnan V. *Linear Matrix Inequalities in System and Control Theory.* SIAM: Philadelphia, PA, 1994.
[23] Zhou K, Doyle JC and Glover K. *Robust and Optimal Control.* Prentice Hall: Englewood Cliffs, NJ, 1996.
[24] Gahinet P. *LMI Control Toolbox for Use with MATLAB.* MathWorks Inc.: Natick, MA, 1995.
[25] Grant M and Boyd S. CVX: Matlab software for disciplined convex programming (web page and software). http://stanford.edu/~boyd/cvx [June 18 2008].
[26] Franklin GF, Powell JD and Workman ML. *Digital Control of Dynamic Systems.* Addison-Wesley: Menlo Park, CA, 1998.
[27] Kurino H, Tagami J, Shimizu K and Kobori T. Switching oil damper with built-in controller for structural control. *Journal of Structural Engineering* 2003; **129** (7): 895-904.
[28] Burl JB. *Linear optimal control : H_2 and H_∞ methods.* Addison Wesley Longman: Menlo Park, CA, 1999.
[29] Spencer BF, Jr., Christenson RE and Dyke SJ. Next generation benchmark control problem for seismically excited buildings. *Proceedings of the 2nd World Conference on Structural Control*. Kyoto, Japan, June 29 - July 2, 1998.
[30] Hatada T, Kobori T, Ishida M and Niwa N. Dynamic analysis of structures with Maxwell model. *Earthquake Engineering & Structural Dynamics* 2000; **29** (2): 159-176.